metals

MDPI

Article

Tensile and Fracture Behavior of Bi-Containing Alloy Sintered on SAE 1010 Steel Sheet

Seung-Hyon Song [1], Chang-Soon Lee [1], Tae-Hwan Lim [1], Auezhan Amanov [2,*] and In-Sik Cho [1,*]

[1] Department of Advanced Materials Engineering, Sun Moon University, Asan 31460, Korea
[2] Department of Mechanical Engineering, Sun Moon University, Asan 31460, Korea
* Correspondence: avaz2662@sunmoon.ac.kr (A.A.); mbrosia1018@naver.com (I.-S.C.); Tel.: +82-41-530-2870 (I.-S.C.)

Abstract: The purpose of this study is to investigate the fractural behavior of lead (Pb)-free material containing bismuth (Bi) that was developed to replace the Pb included in sintered copper (Cu)-based alloy for plain bearings. Mechanical properties and microstructure of two different sintered Cu-based alloys (CuSn10Pb10 and CuSn10Bi7) were compared and analyzed. Under tensile load, a CuSn10Pb10 layer is decomposed into powder and changed to form pores leading to an expansion. Therefore, even after tensile elongation, the matrix itself did not stretch, with no work hardening. However, in the case of CuSn10Bi7, a Bi kept its original shape, resulting in it being the same length as the steel plate, where the hardness and strength increased due to the effect of work hardening. These results suggested that the performance of the alloys was different under a high tensile load, where plain bearings usually undergo tensile deformation.

Keywords: Cu-base alloy; sintering; fracture; dynamic Young's modulus; bushing; bearing

Citation: Song, S.-H.; Lee, C.-S.; Lim, T.-H.; Amanov, A.; Cho, I.-S. Tensile and Fracture Behavior of Bi-Containing Alloy Sintered on SAE 1010 Steel Sheet. *Metals* **2022**, *12*, 1806. https://doi.org/10.3390/met12111806

Academic Editors: Irena Paulin and Crtomir Donik

Received: 16 September 2022
Accepted: 20 October 2022
Published: 25 October 2022

1. Introduction

A plain bearing is the simplest type of bearing, consisting of a bearing surface with no rolling elements, where the journal slides over the bearing surface. Plain bearings must be manufactured from durable material with low friction and high wear and corrosion resistance. The bushing is an independent plain bearing inserted into a housing to provide a bearing surface for rotary application. When Cu- or Al-base alloys operate under oil-lubricated conditions, they can be problematic when the material is used as inserted bushes or shells without a steel backing. Temperature changes cause the loss of interference fit in ferrous housing or significant changes in operating clearance when in non-ferrous housing. The goal is to prevent the loss of interference with ferrous housing and bimetal manufactured by sintering bronze powder on the steel plate [1,2].

Bearing materials containing Pb (lead) are widely used in automotive parts, earth-moving equipment parts, and heavy equipment industries. The chemical composition of C93700 wrought alloy is 80% Cu, 10% Sn, and 10% Pb. Steel-backed Cu or Cu–Pb–Sn materials manufactured by powder metallurgy (P/M) are also used to replace solid bronze bearings [3–5]. Hardness, tensile strength, elongation, etc. have been evaluated for mechanical properties. However, it is known that evaluating the microstructure and mechanical properties in conjunction helps us to understand the wear process. The coefficient of friction (COF) measurement during the wear test is also a critical property [6–10].

The tribological function of a Pb-containing plain bearing reduces the wear by forming an oxidized Pb-enriched layer. The wear was more severe than in the case of unleaded bronze when no such film was developed. Pb particles are oxidized and solidified after melting by friction heat, and the spreading of lead over the contact surface may rely on selective wear of the bronze phase. During sliding, bronze and Pb particles are detached from the base material. Pb-enriched flakes can further oxidize due to frictional heating, leading to the mixed Cu–Pb oxide layer. In addition, since a certain percentage of oxygen

formed in the sintering process is included in the sintering layer, it can be seen that forming an oxidized Pb-enriched layer is promoted when frictional heat is generated. Oxidative wear is also known as the main wear mechanism in a sliding wear test conducted on a material in which soft materials, such as Sn, Pb, Bi, and Sb, are dispersed in an intrinsic high entropy alloy (HEA) matrix [11–13].

To develop Pb-free materials, many studies have been conducted on the reinforcement of bearing materials [14–20]. It has been previously reported that the COF and the wear amount of Cu-based sintered bearing material were reduced by ultrasonic nanocrystalline surface modification (UNSM) technology [21,22]. The Al–Sn matrix product is another type of sliding bearing which contains Pb. In the Al–Sn matrix, when Bi is added, it forms a solid solution with Sn, causing the solid solution to strengthen and increase in hardness. However, in the case of Pb, there is no increase in hardness in the mixed phase with Sn. Therefore, additional research is needed to maintain the soft phase when Bi is added [23,24]. In this study, the tensile fracture mechanisms were compared and analyzed for sliding bearing materials containing Pb and Bi to understand the role of Pb in the alloy in order to improve the performance of Pb-free alloys.

2. Materials and Methods

Two types of Cu-based bimetals (CuSn10Pb10 and CuSn10Bi7) manufactured by the sintering process were prepared. After spreading bronze powder on the cold-rolled steel plate made of SAE 1010, the material that went through the sintering process was tested. The sintering process was performed at 800–900 °C. Bi was selected as the alloy composition of the Pb-free material because it is known as an element with similar properties to Pb and is also harmless to the human body. The specimens were machined from the sintered strips. The dynamic Young's modulus of the specimens with precise dimensions shown in Figure 1 was measured in accordance with ASTM E 1876-01 standard, which measures the velocity of longitudinal and transverse waves to measure the Young's modulus, shear modulus, and Poisson's ratio. The elastic wave velocity was measured using an impulse excitation technology (IET) method. In order to accurately find the natural frequency denominator of the material, a general specimen with a square shape is placed on the node line wire and the impulse point is hit using the impulse tool. The signal is received through a non-contact microphone to measure the flexural frequency, and the dynamic elastic modulus can be easily calculated by substituting it into the related expression [25].

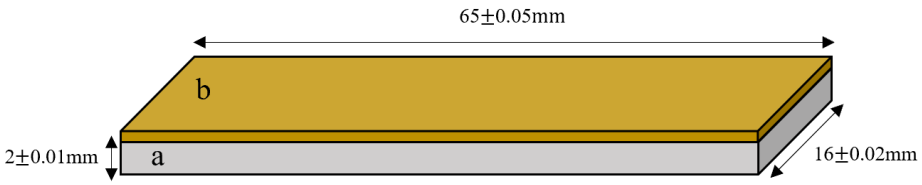

Figure 1. Schematic view of the dynamic Young's modulus specimens.

Tensile test specimens were fabricated with the dimensions shown in Figure 2. The tensile test was performed using a universal test machine (QM100T, QMESYS, Komachine, Yongin, Korea) at 1 mm/min. The fracture surface and cross-sections were observed using a scanning electron microscope (SEM: JSM-7500F, JEOL, Akishima, Japan). The internal changes that occurred during the tensile process in the sintered layer were also observed by SEM. The chemical composition of the fractured surface was analyzed using energy-dispersive X-ray spectroscopy (EDS). In addition, the cross-sections of the sintered strip and sintered layer were observed using an optical microscope (OM: MF-A1010, Mitutoyo, Kawasaki, Japan). The micro-hardness was measured using a Vickers hardness tester at a load of 100 gf (Micromet3, Buehler, IL, USA). The Young's modulus, shear modulus, and Poisson's ratio of the specimens were measured using a dynamic measurement device,

shown in Figure 3. The following Equation (1) is the relationship between the Young's modulus and the natural frequency, density, and length of the specimen.

$$2fl = \sqrt{\frac{E}{\rho}} \tag{1}$$

where f is the natural frequency of the material, l is the length of the specimen, ρ is the density, and E is the Young's modulus.

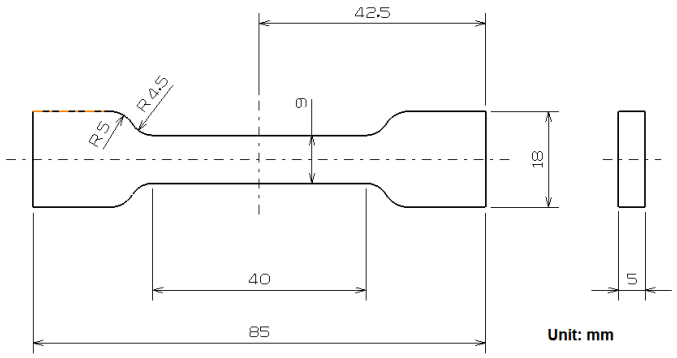

Figure 2. Schematic view of the tensile test specimens.

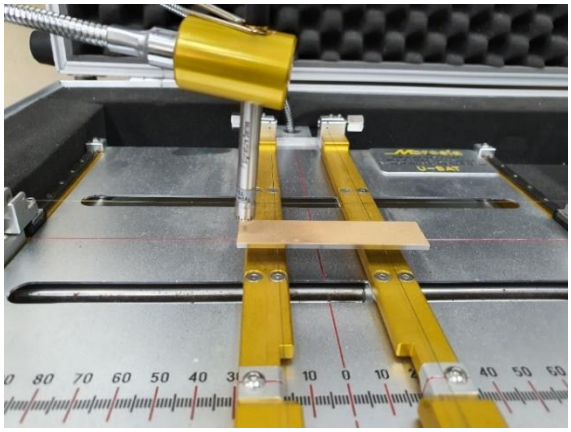

Figure 3. Dynamic Young's modulus tester.

3. Results

3.1. Microstructure

Cross-Sectional OM and Top Surface SEM Images

The cross-sectional OM images of the sintered strips are shown in Figure 4. The structure of the steel part consists of fine ferrite and pearlite. The grain size of ferrite is very fine, due to the rolling process, and some grain growth has occurred during the sintering process. The top sintered layer consists of a yellow matrix and black areas visible as pores. Although the sintered layers showed similar structures, there is a difference in the number of pores. The distribution of pores is quite dense in the Pb sintered layer, and the Bi sintered layer is distributed at relatively wide intervals. The sintered layer comprises a matrix structure, pores, and an alloy component of the second phase, as confirmed by SEM images shown in Figure 5. The pore and the alloy composition zone of the Bi sintered layer are wider than the Pb sintered layer. It is believed that the growth of Bi occurred more during the sintering process due to the sintering temperature and time. The red arrow A indicates the pore, and the blue arrow B indicates the alloy composition zone. The ratio of the porosity and alloy components was calculated using a digital image analyzer to photograph the SEM images, and the results are listed in Table 1. The small amount of pores

is more densified in the sintering process, and the result is consistent with the measurement of higher density of the Bi sintered strip. This is related to the temperature and time of the sintering process. In general, the longer the sintering time, the more densification occurs.

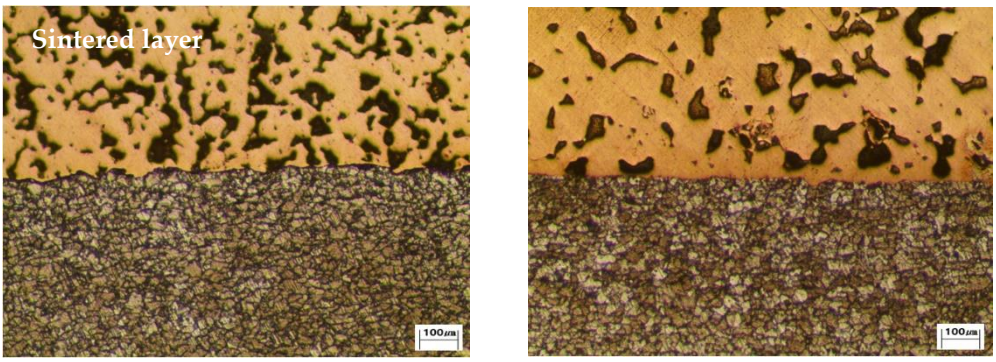

(**a**) (**b**)

Figure 4. Cross-sectional OM images of Pb and Bi sintered strips (×100). (**a**) Pb, (**b**) Bi.

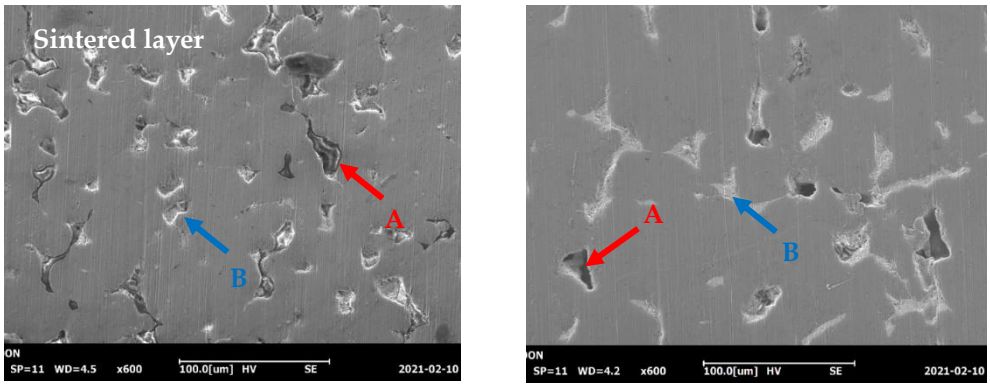

(**a**) (**b**)

Figure 5. SEM Microstructures of the sintered layer. The red arrow A indicates the pore, and the blue arrow B indicates the alloy composition zone. (**a**) Pb sintered strip, (**b**) Bi sintered strip.

Table 1. Ratio of pores, alloy components, and matrix of the sintered layers in wt.%.

	Pb Sintered Layer	Bi Sintered Layer
Matrix	91.61	94.32
Porosity	6.08	1.35
Alloy	2.31	4.32

The chemical composition of the alloy zone is listed in Table 2. In the alloy zone of the Pb sintered layer, only the Pb was detected, as shown in Figure 6a. In the case of the Bi sintered layer, a small amount of Cu peak was observed in the alloy zone, where the main composition was Bi (see Figure 6b). It is thought that both Pb and Bi exist as a single phase in the alloy zone within the matrix. However, slight peaks of Cu and Sn, shown in Table 3, appeared due to the influence of the matrix around the Bi region during electron beam irradiation. Pb and Bi elements were not detected in the matrix for both Pb and Bi sintered layers (see Figure 7). This may be attributed to the fact that Cu and Pb have limited solubility limits with each other. Pb and Sn become entirely liquid at a sintering temperature of 800–900 °C, where the liquid phase sintering is performed with Cu powder. It is challenging for Cu to form a solid solution with Pb, so it is considered that a Cu–Sn compound is formed during the solidification process, and Pb is precipitated as a single phase. Similarly, Cu and Sn were mainly detected in the matrix structure of the Bi sintered layer, but Bi was not detected. A small amount of Zn was detected. It has been earlier

reported that the presence of Zn can reduce the COF and increase the matrix hardness [26]. OM, SEM, and EDS analyses confirmed that the Pb and Bi sintered layers consist of matrix and alloy element regions and pores. The matrix was composed of Cu and Sn, confirming that Pb and Bi alloy compositions did not form a compound and existed as a single phase. In other words, the functions of Pb and Bi in the sintered alloy for sliding bearings are performed as a single phase. It is important to confirm the function of this single phase in the lubrication process. The slight differences in the Pb and Bi sintered layers are the amount, distribution, and size of pore and alloy elements. It can be assumed that this is due to the difference in sintering process conditions. It is known that the longer the sintering time and the higher the sintering temperature, the faster the pore growth occurs and the higher the density. Accordingly, the sintering process temperature of the Bi sintered layer was increased, and the sintering time was long [20].

Table 2. Chemical composition of alloy zone in wt.%.

	Pb	Bi	O	Cu
Pb-sintered layer	89.87	Not detected	10.13	Not detected
Bi-sintered layer	Not detected	93.70	2.78	3.52

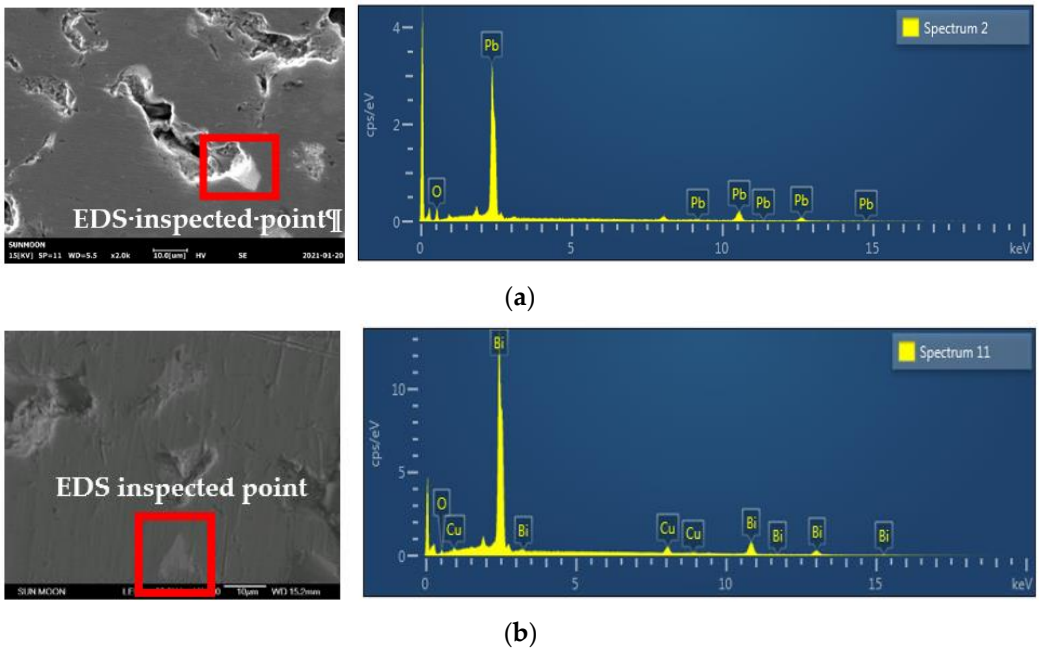

Figure 6. SEM-EDS results of Pb and Bi areas on sintered layers. (**a**) Pb-sintered layer, (**b**) Bi-sintered layer.

Table 3. Chemical compositions of the matrix in wt.%.

	Cu	Sn	O	Others
Pb-sintered layer	73.86	7.10	1.50	Balanced: C
Bi-sintered layer	85.97	9.77	1.60	Balanced: Zn (2.67)

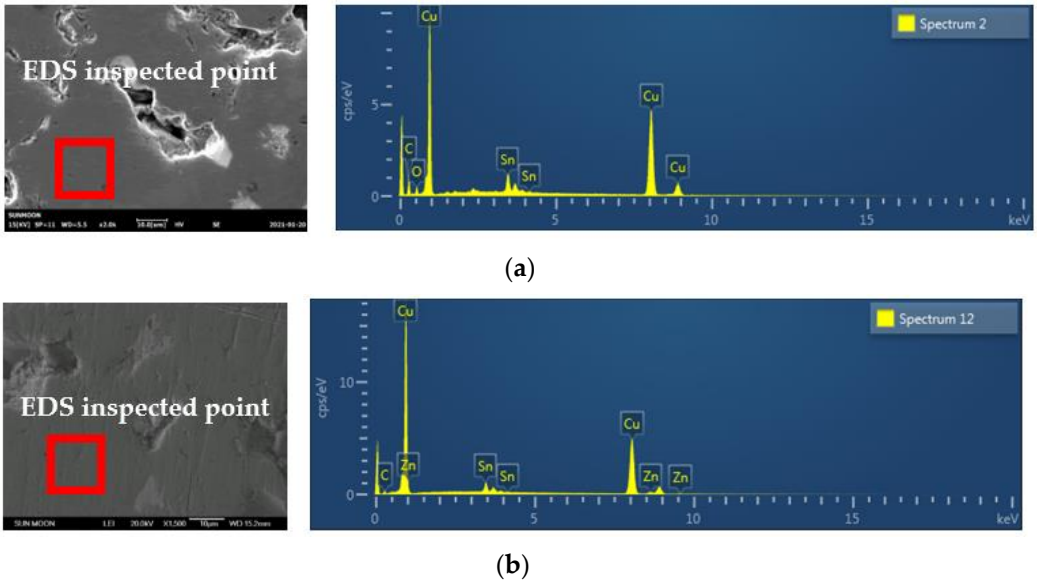

Figure 7. SEM-EDS results of matrix areas of Pb and Bi sintered layers. (**a**) Pb sintered layer, (**b**) Bi sintered layer.

3.2. Dynamic Young's Modulus

As the length of the specimens is the same, the Young's modulus increases with increasing density and natural frequency. The density of the specimens is reported in Table 4. As a result of the dynamic elasticity test, the Young's and shear moduli of the Bi sintered layer were found to be higher than those of the Pb sintered layer by about 17.6% and 9.8%, respectively. The Poisson's ratio was also obtained by the dynamic elasticity test method. The relationship between the Young's modulus, the shear modulus, and Poisson's ratio follows the equation below:

$$E = 2G\,(1 + \mu) \tag{2}$$

where E is the Young's modulus, G is the shear modulus, and μ is the Poisson's ratio.

Table 4. Dynamic Young's modulus test results.

	Density (g/cm^3)	E_{dy} (GPa)	G_{dy} (GPa)	Poisson's Ratio
Pb sintered layer	7.761	138.97	56.67	0.226
Bi sintered layer	8.101	163.55	62.23	0.314
Ratio (Pb/Bi)	4.3% (Bi is high)	17.6% (Bi is high)	9.8% (Bi is high)	38% (Bi is high)

The Young's modulus measurement test results are listed in Table 4. The high Young's and shear moduli mean that the stress is required to increase the strain in the region below the proportional limit. However, a high Poisson's ratio implies that the ratio of transverse strain to axial strain is high. A material with a high Poisson's ratio has a higher transverse strain for the same amount of axial strain as a material with a low Poisson's ratio. Hence, the dimensional reduction rate in the transverse direction of the Bi sintered layer is higher than that of the Pb sintered layer. Due to the difference in Poisson's ratio, the thickness reduction rate of the Bi sintered layer is considered to be higher even when the tensile strain increases and enters into the plastic region. This thickness reduction amount was verified by measuring the thickness of the sintered layer before and after the tensile test [27]. The Poisson's ratio shows the ratio of vertical deformation to horizontal deformation within elasticity, and it is believed that there will be more deformation in the thickness direction when the same amount of stretching occurs compared to the Pb sintered layer. When moving from an elastic region to a plastic region, the deformation in the thickness direction that occurred in the elastic region is changed to permanent deformation, and it is estimated that the work hardening rate would be high depending on the high deformation rate. As a result, the Young's modulus, shear modulus, and Poisson's ratio of the Bi sintered strip

were higher than that of the Pb sintered strip. Higher Young's and shear moduli mean less strain under the same stress. However, in the Bi sintered strip, the Poisson's ratio was measured to be very high compared to the Pb sintered strip due to the fact that the rate of decrease in the opposite direction from the tensile direction is higher when tensile elongation occurs.

3.3. Tension Test Results

3.3.1. Sintered Surface

Figure 8 shows the fractured specimens after the tensile test. Wide cracks were observed across the entire surface of the Pb sintered layer of the fractured specimen. However, on the surface of the Bi sintered layer, relatively small cracks were observed only around the fracture site. It can be seen that the luster of the surface of the sintered layer was significantly lost, and a lot of fine scratches were generated in the tensile direction. Considering that many wide cracks are generated in the Pb sintered layer, it is thought that the major fracture mechanism is that many cracks are enlarged in the stretching process. The Pb-sintered layer seems to be stretched as the crack expands, while the Bi-sintered layer was estimated to be stretched as the sintered layer itself expands. After the tensile test, the fracture of the sintered layer was observed by SEM, as indicated by a red circle in Figures 9 and 10. The observation position of the surface was as far as possible from the fractured surface, with relatively wide cracks due to the relatively lower amount of deformation. It was confirmed that it can be divided into pore, matrix, and Pb and Bi elements. The fractural behavior of the pores was similar to the Pb and Bi elements, but it differed from the matrix.

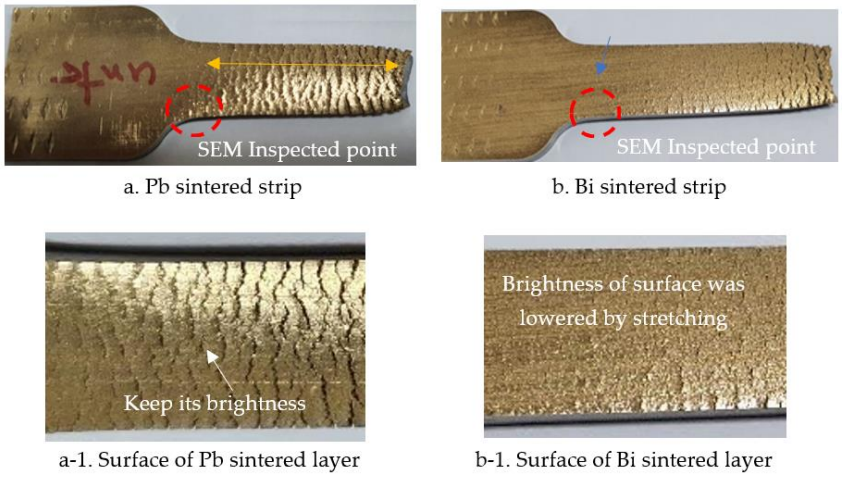

a. Pb sintered strip b. Bi sintered strip

a-1. Surface of Pb sintered layer b-1. Surface of Bi sintered layer

Figure 8. Photography of the specimens after tensile test.

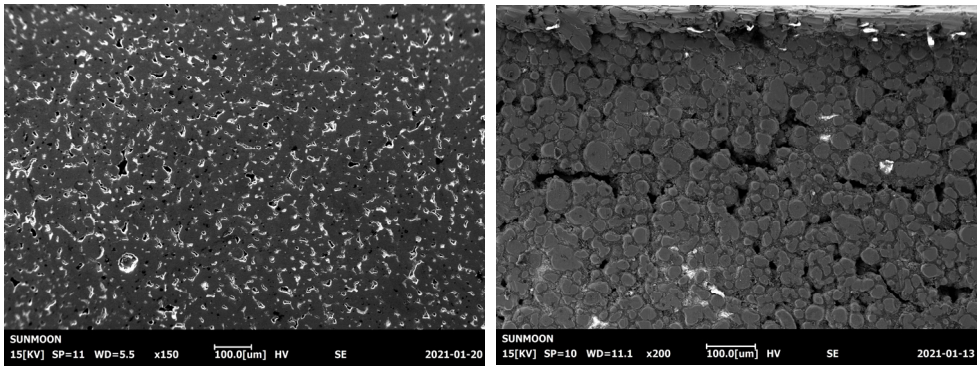

a. Before tensile test b. Pore expansion after tensile test

Figure 9. SEM images of Pb sintered material surface before and after tensile test.

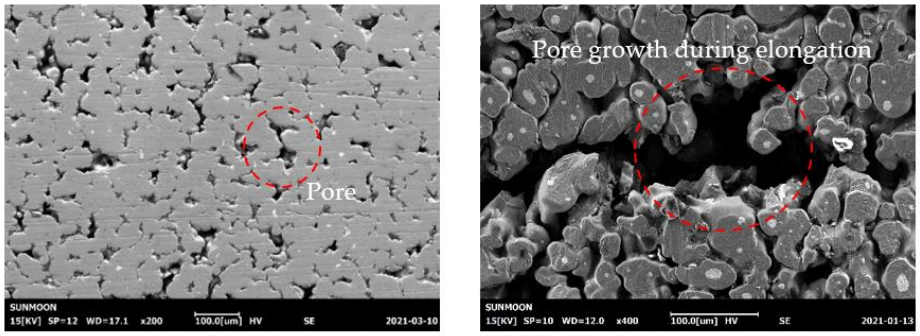

a. Pore before tensile test b. Pore extension after tensile test

Figure 10. SEM images of Bi sintered material surface before and after tensile test.

3.3.2. Pore Behavior

The extension of pores begins when the specimen is stretched in the tensile direction, leading to a formation of interconnected pores with other adjacent ones. According to the notch and shape of the pores, cracks are formed in both horizontal and vertical directions. After the tensile test, the matrix that appears in the form of grains on the surface is considered a crack progressed from the pores. This pore behavior can be observed more clearly by the cross-sectional images shown in Figure 11. Tensile stress is concentrated on large-sized pores, which are enlarged first and, subsequently, form a wide crack. In small-sized pores, the cracks are observed to be propagated inward. In general, sintered materials tend to have pores. In this study, both Pb and Bi-sintered materials showed identical pore growth mechanisms, as illustrated in Figure 12, where the size of the pores in the Pb-sintered layer (approximately 35 μm) was smaller than the Bi-sintered layer (approximately 7 μm). When the sintered layer undergoes the tension stress, the pore extends first. However, after the tensile test, the pores extended and interconnected with small pores having a mean pore length of approximately 120 μm. It can be explained that when the sintering layer bears a load in a tensional direction, the pores receive it first and then subsequently expand.

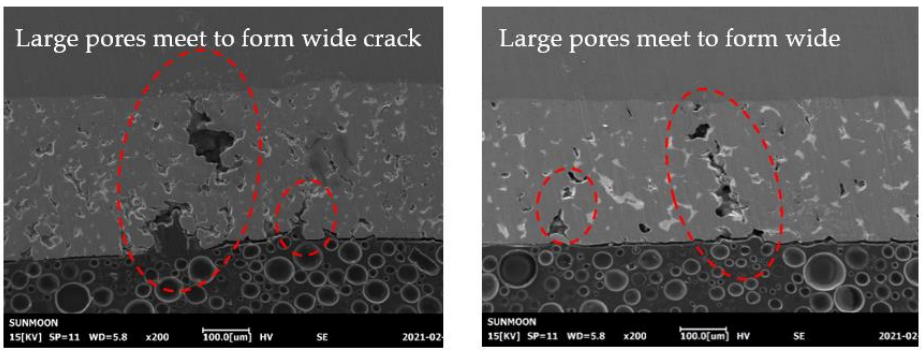

a. Pore before tensile test b. Pore extension after tensile test

Figure 11. Cross-sectional SEM images of Bi sintering material before and after tensile test.

a. Pore before tensile test b. Pore extension after tensile test

Figure 12. Schematic diagram of pore growth and growth direction (↑) during the tensile elongation.

3.4. Alloy Behavior

3.4.1. Pb Sintered Layer

The tensile behavior of Pb and Bi elements in the sintered layer showed a clear difference. It was observed that the Pb component, existing as a single phase inside the sintered layer, was decomposed in the form of powder as the strip was stretched. Here, the matrix of the sintered layer was not stretched, but the Pb element inside the sintered layer was decomposed in the form of powder, and the decomposed Pb area was elongated. This behavior can be confirmed more clearly by high-magnification SEM images, as shown in Figure 13. It can be seen that the matrix is in the form of circular grains, and the powder forms concaves around it. This can be explained by the schematic diagram shown in Figure 14. The behavior of the Pb decomposition form can be confirmed more clearly, as shown in Figure 15. It can be observed that a large number of new pores appeared inside the sintered layer after the tensile test. These pores are much larger than the pores in the original sintered state due to the expansion of the pores as the Pb area is decomposed into powder form. Decomposed Pb powder was attached to the interface of the newly formed pores, and it was presumed that the decomposed Pb powder acted as an adhesive for the sintered layer.

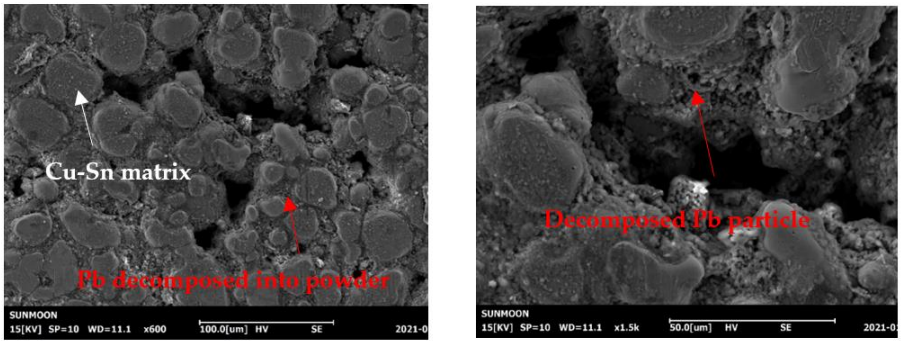

a. Extended matrix b. Matrix and decomposed Pb particle

Figure 13. SEM image of the elongated Pb sintered layer.

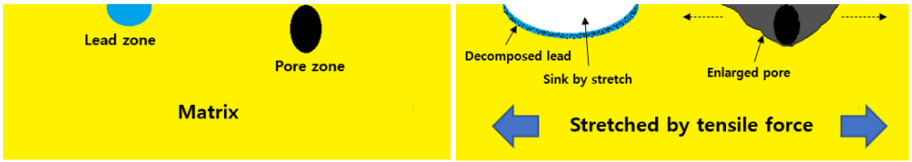

a. Before tensile test b. After tensile test

Figure 14. Schematic diagram of the Pb decomposition behavior.

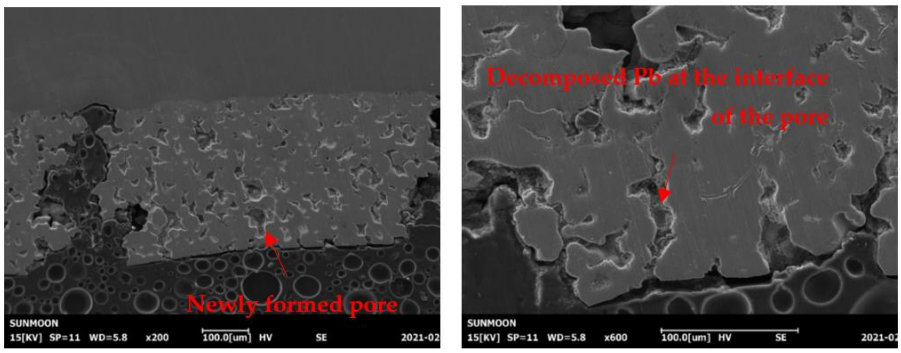

a. New pores b. Decomposed Pb particle

Figure 15. Cross-sectional SEM images of the elongated Pb sintered layer.

3.4.2. Bi-Sintered Layer

Figure 16 confirmed that the Bi-sintered layer did not decompose after the tensile test and remained as a single phase. For this reason, when the upper surface of the sintered layer after the tensile test was observed, the grain shape generated by crack propagation from the pores and the elongated Cu–Sn matrix can be seen. Hence, in the Bi-sintered layer, unlike the Pb-sintered layer, sinking around the matrix was not observed. In the case of the Pb-sintered layer, when tensile elongation occurs, the Pb or pores are expanded as the main elongation mechanism. In the case of the Bi-sintered layer, the entire sintered layer is stretched evenly during the tensile test, as the Bi is not decomposed. Figure 17 shows the cross-sections of the Bi sintered layer. The crack proceeded in the same way with the pore, and the extension of the pore occurred due to tensile elongation, as shown in Figure 18.

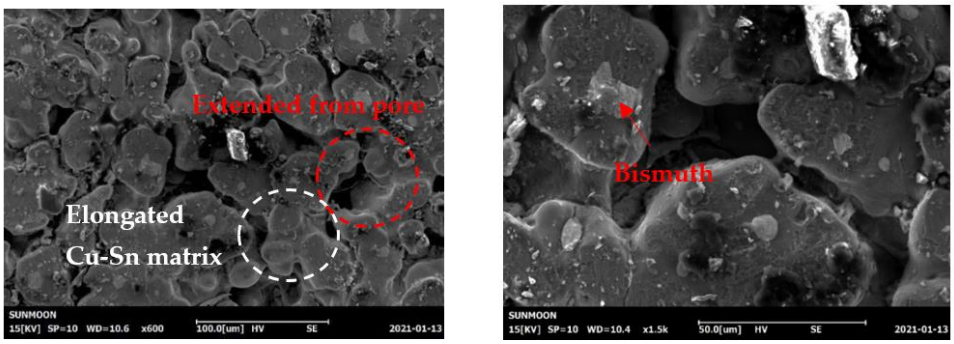

a. Extended Cu-Sn matrix b. Undecomposed Bi

Figure 16. SEM images of the elongated Bi sintered layer.

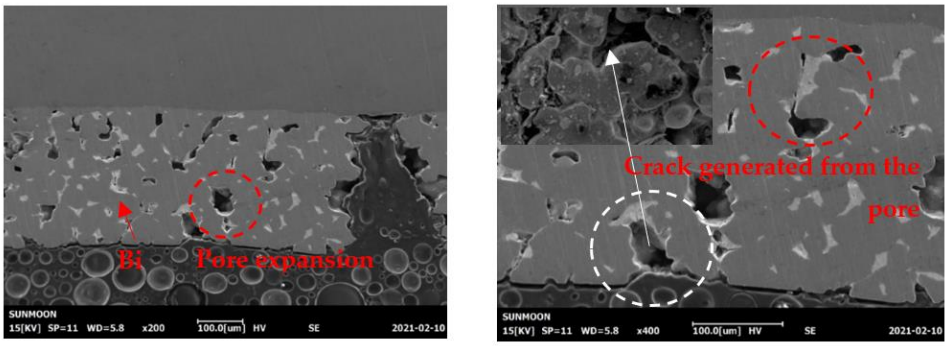

a. Undecomposed Bi b. Pore expansion and generated crack

Figure 17. Cross-sectional SEM images of the elongated Bi-sintered layer.

a. Before tensile test b. After tensile test

Figure 18. Schematic view of the elongated Bi-sintered layer.

3.4.3. Tension Fracture Surface

Figure 19 shows the photography of the fractured surface of the Pb- and Bi-sintered layers. It was confirmed that the fracture surface of the steel back of the Pb is bent in a C-shape. This bending phenomenon is not a decrease in thickness, and it occurred due to the different elongation rates between the sintered layer and the steel plate. Figures 20

and 21 show the steel back and the sintered layer simultaneously at low and high magnifications, respectively. It can be seen from Figure 21a that many circular particles are observed, while very fine point-shaped particles are attached around the circular particles. Based on the high-magnification SEM image shown in Figure 21b, the fractured surface mechanisms were three types: (1) the spherical particle surface remains as it is (arrow A); (2) the spherical particle surface is torn—outward form (arrow B); (3) the formation of very fine powder particles (arrow C). The shape in which the spherical particle shape indicated in (A) remained on the surface is presumed to keep the original shape due to the surrounding pores. The torn form (B) is estimated to be the final fractured form as the sintered matrix is stretched. The shape of (C), with fine powder particles attached, is not torn and maintains a circular shape similar to that of (A). (C) Fine powder particles attached to the shape were analyzed by EDS. The decomposition of the Pb particles during the tensile stretching process played an important role in protecting the shape of the Cu–Sn matrix from being torn.

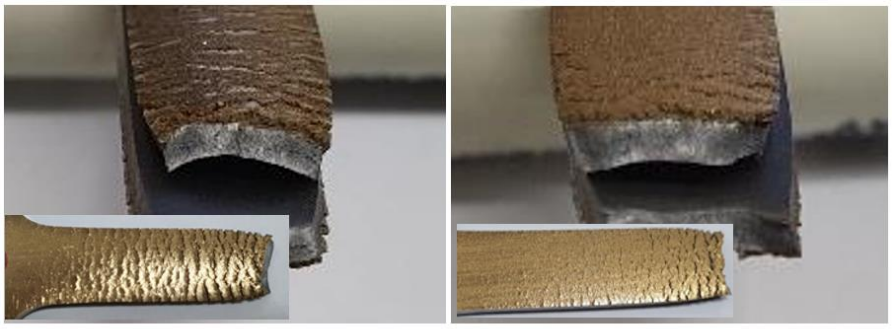

a. Pb sintered strip b. Bi sintered strip

Figure 19. Photography of the fracture surface of Pb- and Bi-sintered layers.

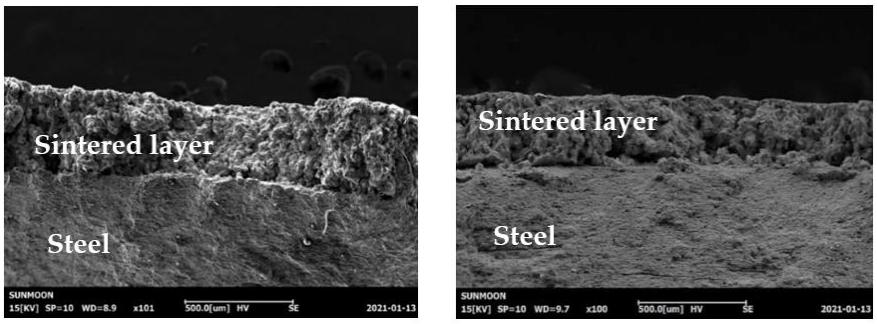

a. Fractured surface of the Pb-sintered layer b. Fractured surface of the Bi-sintered layer

Figure 20. SEM images of the fractured surface of Pb- and Bi-sintered layers.

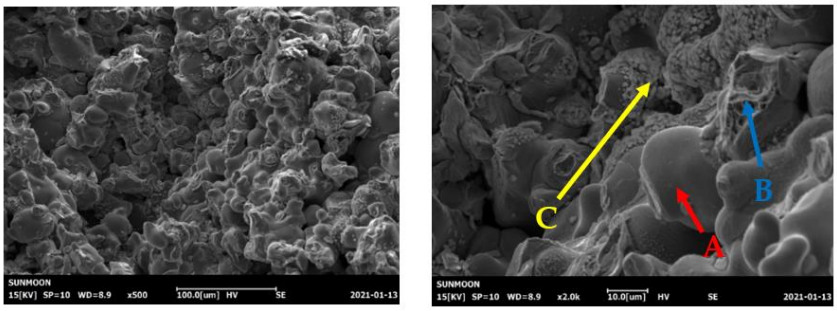

a. Fractured specimen b. High-magnification SEM image;

Figure 21. SEM images of the fractured surface of the Pb-sintering layer. Spherical particle surface (arrow A); outward form (arrow B); very fine powder particles (arrow C).

The fractured surface of the Bi-sintered strip differed from that of the Pb-sintered strip. As shown in Figure 22, the circular particle shape is hardly visible on the fracture surface of the Bi-sintered layer. The area indicated by the blue arrow shows a fractured surface in the form of being torn due to tensile elongation. In the Pb-sintered layer, it was confirmed that most of the fracture fronts maintain a spherical shape, but in the Bi-sintered layer, most of the fractures appeared as a torn fracture surface due to the stretching of the sintered layer. The difference in fractured surfaces is the functional difference between Pb and Bi inside the sintered layer. Pb is decomposed during the tensile stretching and remains on the Cu–Sn surface. It is believed that the decomposed Pb protects the Cu–Sn matrix from stretching during the tensile stretching. However, Bi maintains its original shape without deformation inside the matrix during tensile stretching. Therefore, the Cu–Sn Matrix was also elongated in the same amount as the tensile elongation of the steel back. Figures 23 and 24 show the schematic diagrams of the Pb- and Bi-sintered layers under tensile stretching. In the case of the Pb-sintered layer, new pores were formed due to the stretching of the steel back, and they were interconnected to form many wide cracks and pores. In the case of the Bi-sintered layer, the presence of Bi maintains its original shape in tensile behavior, which led to similar behavior and length to the steel back.

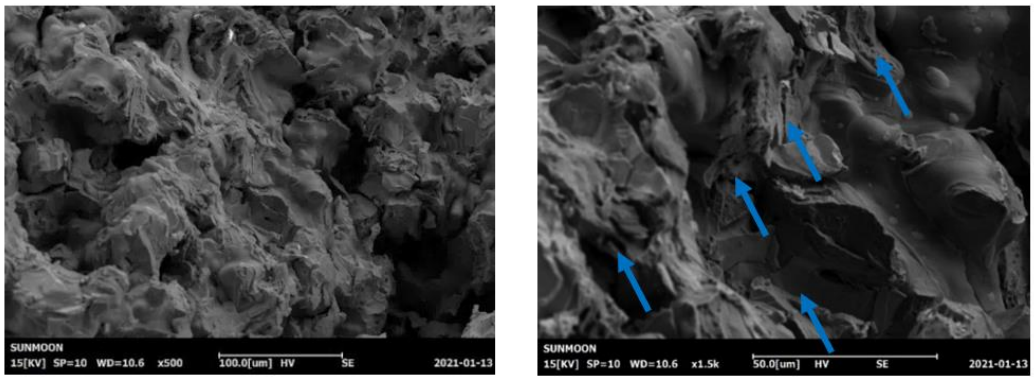

a. Fractured Bi sintered layer b. High-magnification SEM

Figure 22. SEM images of the fractured Bi-sintered layer. Blue arrows indicate the fractured surface.

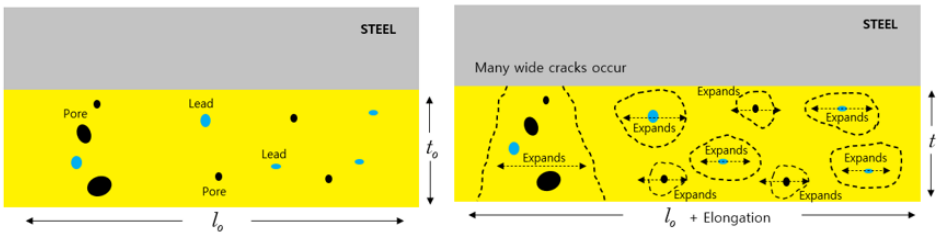

a. Before tensile test b. After tensile test

Figure 23. Schematic diagram of the behavior of Pb during tensile elongation.

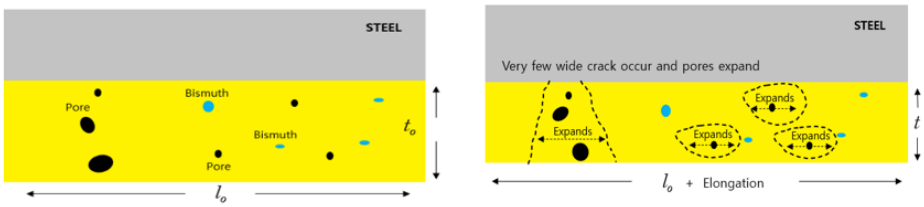

a. Before tensile test b. After tensile test

Figure 24. Schematic diagram of the behavior of Bi during tensile elongation.

3.4.4. Hardness of the Pb-Sintered Layer

It is a challenge to accurately measure the hardness of the sintered materials due to the presence of pores and elements of other phases. Several points were measured in order to obtain reliable hardness data of the Cu–Sn matrix. Figure 25 shows the SEM image of the accurate Vickers indenter mark on the Cu–Sn matrix with the pores and alloying elements. Figure 26 shows the Vickers indenter mark on the Cu–Sn matrix without pores and alloying elements. The surface hardness of the Pb and Bi sintered layers was about 85 ± 13 and 102 ± 18 HV, respectively. Actually, the hardness of these types of sintered layers is in the range of 80–100 HV. For example, it has been earlier reported that the hardness of the Pb sintered layer was about 103 HV [28].

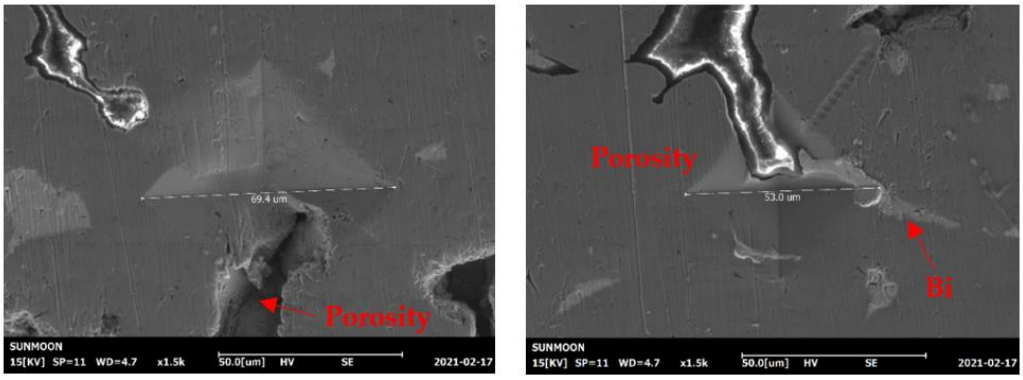

a. Indentation mark at porosity b. Indentation mark at porosity and Bi

Figure 25. SEM images of the Vickers hardness indentation marks.

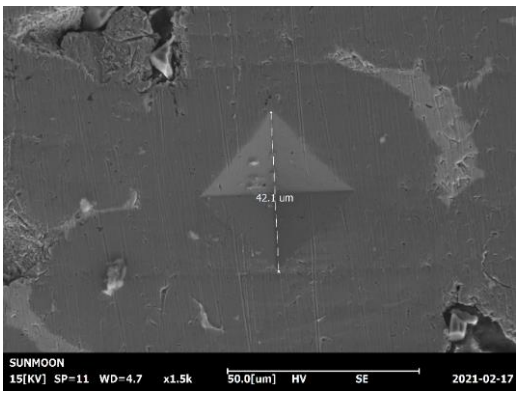

Figure 26. SEM images of the Vickers indentation mark on the surface of the Cu–Sn matrix.

3.4.5. Stress–Strain Curve

Figure 27 shows the tensile test results of the Pb- and Bi-sintered strips. It can be seen that in the Pb-sintered strip, the yield point drop appears as in mild steel. There are two possible reasons for the yield point descent phenomenon: (1) as the steel back is mild steel, it can be assumed that the phenomenon is typically produced by mild steel; (2) the effect of pores in the sintered layer. As plastic deformation begins past the upper yield point, cracks occur at the sharp notch of the pores inside the sintered layer and progress, so it can be estimated that elongation occurs even at a stress much lower than the upper yield point. However, as the thickness of the steel plate is much thicker than the thickness of the sintering layer, the yield point drop of mild steel is considered to be the main reason, where the presence of pores accelerated the process. In the Bi-sintered strip, the yield point drop does not occur. It can be seen that the stress rises with a low slope as the yield point passes and then goes to the typical plastic deformation region, and the stress rises to the ultimate tensile strength (UTS). However, the stress gradually rises without the yield point

drop phenomenon, as the plastic deformation of the sintered layer as it passes through the elastic region plays a large role. The stress is gradually increased due to the sum of the stress reduction in the yield point drop, and the stress increases due to work hardening, as work hardening occurs a lot as soon as the yield point drop starts. For this reason, the Bi-sintered strip enters the plastic region without the yield point phenomenon. In contrast, the Pb-sintered strip does not enter the plastic region under the lower yield point stress up to about a 1 mm section along with the yield point phenomenon. Tensile test results of the Pb- and Bi-sintered strips are listed in Table 5. The UTS of the Bi-sintered strip was 397 MPa, which was about 9% higher than the 365 MPa of the Pb-sintered strip. This difference is due to the work hardening rate of the sintered layer.

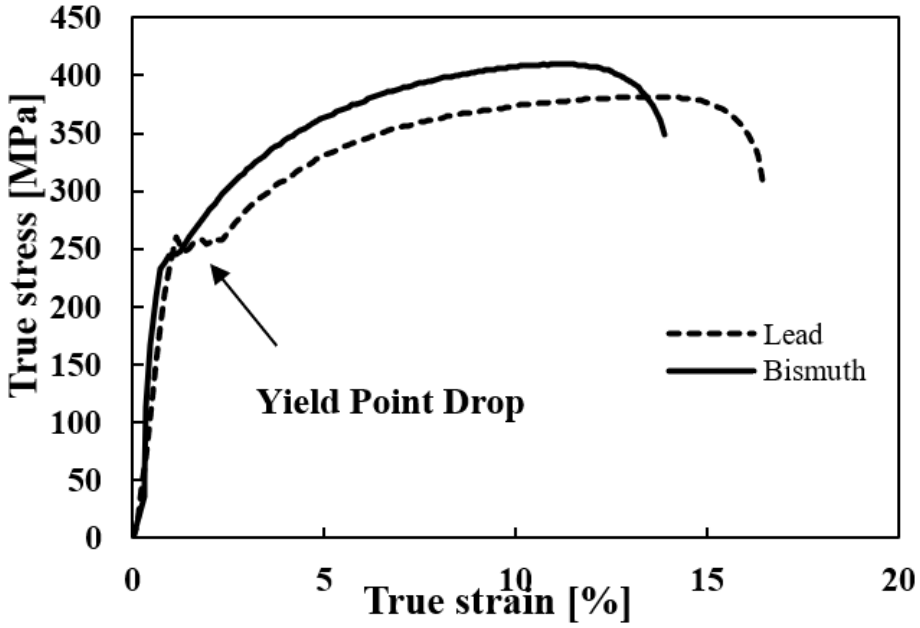

Figure 27. Stress–strain curves of the Pb- and Bi-sintered strips.

Table 5. Tensile test results of the Pb- and Bi-sintered strips.

	Yield Strength (MPa)	Ultimate Tensile Strength (MPa)	Elongation (%)	Toughness (J/mm^3)
Pb sintered layer	268	365	14.1	106.5
Bi sintered layer	251	397	16.5	132.9

It is evaluated that the difference in the behavior of Pb and Bi components in the sintered layer affects the operating environment of the bearing. There are various environments in the operating environment of bearings. For example, there are applications to reduce friction and wear on shafts in very low-load environments, and there are bearings that are mounted on heavy-duty equipment, such as construction equipment and earthmoving equipment. A shaft that handles such a heavy weight is subjected to a high load, and deformation occurs according to its operation. When the shaft is deformed, the bearing is also deformed, and, according to this deformation, tensile elongation occurs in the bearing. In such an environment, as the sintered layer is stretched, performance changes occur according to the behavior of Pb and Bi. It is generally known that as the strength and hardness of a material increase, both ductility and toughness decrease. In the Bi-sintered layer, the increase in strength and hardness according to tensile elongation is higher than that of the Pb-sintered layer, so it is considered that the decrease in ductility and toughness of the Bi-sintered layer is high under the tensioned condition. When the ductility and toughness are lowered, the material can be easily damaged by an impact load.

4. Conclusions

In this study, the tensile and fracture behavior of the Pb and Bi sintered layers were comparatively analyzed. It was confirmed that the Young's modulus, shear modulus, and surface hardness were higher in the Bi sintered strip than in the Pb sintered strip. Higher properties of the Bi sintered strip have the potential to improve performance during friction and wear compared to the Pb sintered strips. However, based on the tensile properties, the two Pb and Bi sintered layers showed markedly different behavior. Therefore, in order to develop a Pb-free material that completely replaces the Pb, the friction and wear characteristics of the bearings under stretching need to be comprehensively evaluated.

Author Contributions: Conceptualization, S.-H.S., I.-S.C. and T.-H.L.; methodology, S.-H.S., C.-S.L.; validation, I.-S.C., T.-H.L. and A.A.; formal analysis, S.-H.S.; investigation, S.-H.S., I.-S.C. and A.A.; writing—original draft preparation, S.-H.S., I.-S.C. and A.A.; writing—review and editing, I.-S.C. and A.A.; supervision, T.-H.L., I.-S.C. and A.A.; project administration, I.-S.C., A.A. and C.-S.L.; funding acquisition, I.-S.C., A.A. and C.-S.L. All authors have read and agreed to the published version of the manuscript.

Funding: This research was supported by the National Research Foundation of Korea(NRF) funded by the Ministry of Education, Science and Technology (grant number 202001290001 and 20210131001). This research was funded by the Industrial Technology Innovation Development Project of the Ministry of Commerce, Industry and Energy, Rep. Korea, grant number 20010482.

Data Availability Statement: Not applicable.

Conflicts of Interest: The authors declare no conflict of interest.

References

1. Waterman, N.A.; Ashy, M.F. *The Material Selector*; Chapman & Hall: London, UK, 1997; p. 1.
2. Xiao, J.; Qin, W.; Xu, S. Interference and thickness design of bushing of connecting rod small end for Anti-loosing. *Eng. Fail. Anal.* **2021**, *127*, 105556. [CrossRef]
3. Totten, G.E. Friction, Lubrication, and Wear Technology. In *ASM Handbook*; ASM International: Novelty, OH, USA, 2017; p. 18.
4. Davis, J.R. Copper and Copper Alloys-Properties of Cast Copper Alloys. In *ASM Specialty Handbook*; ASM International: Novelty, OH, USA, 2001; p. 7.
5. Lee, P.W.; Trudel, Y.; Lacocca, R.; German, R.; Ferguson, B.; Eisen, W.; Moyer, K.; Madan, D.; Sanderow, H. Powder Metal Technologies and Applications-Copper Powder Metallurgy Alloys and Composites. In *ASM Handbook*; ASM International: Novelty, OH, USA, 1998; p. 7.
6. Prasad, B.K. Sliding wear behavior of bronzes under varying material composition, microstructure and test conditions. *Wear* **2004**, *257*, 110–123. [CrossRef]
7. Gebretsadik, D.W.; Hardell, J.; Prakash, B. Friction and wear characteristics of different Pb-free bearing materials in mixed and boundary lubrication regimes. *Wear* **2015**, *340–341*, 63–72. [CrossRef]
8. Wollmann, T.; Nitschke, S.; Klauke, T.; Behnisch, T.; Ebert, C.; Füßel, R.; Modler, N.; Gude, M. Investigating the friction, wear and damage behaviour of plain bearing bushes of the variable stator vane system. *Tribol. Int.* **2022**, *165*, 107280. [CrossRef]
9. Aravind, T.V.; Arul, S. Effect of deep cryogenic treatment on C93700 bearing bush material used in submersible pumps. *Mater. Today Proc.* **2021**, *46*, 4685–4690. [CrossRef]
10. Rodichev, A.; Novikov, A.; Gorin, A.; Tokmakova, M. Analysis of the wear resistance of a hard anti-friction coating, applied to a plain bearing, under the conditions of boundary friction. *Transp. Res. Procedia* **2021**, *57*, 573–580. [CrossRef]
11. Equey, S.; Houriet, A.; Mischler, S. Wear and frictional mechanisms of copper-based bearing alloys. *Wear* **2011**, *273*, 9–16. [CrossRef]
12. Kim, C.K. SEM/EDX Analysis on the Composition and Surface Defect in a Pin Bushing Bearing for an Automotive Engine. *J. KSTLE* **2007**, *23*, 195–200.
13. Yadav, S.; Kumar, A.; Biswas, K. Wear behavior of high entropy alloys containing soft dispersoids (Pb, Bi). *Mater. Chem. Phys.* **2018**, *210*, 222–232. [CrossRef]
14. Kuhn, H.-A.; Koch, R.; Knab, M. Thermal stability of lead-free wrought Cu-base alloys for automotive bushings. *World Metall. ERZMETALL* **2007**, *60*, 199–207.
15. Weber, K.; Pucher, K. Neuer Pb-freier Kupferwerkstoff für Gleitlageranwendungen in Verbrennungsmotoren und Getrieben. *Metall* **2009**, *63*, 564–567.
16. Pucher, K.; Weber, K.; Huk, V.; Kuhm, H.-A. *Entwicklung Pb-Freier Lagerwerkstoffe Für Hochbelastete Monometall-Gleitlager*; Tribologie-Fachtagung: Gottingen, Germany, 2009.
17. Zoghipour, N.; Tascioglu, E.; Atay, G.; Kaynak, Y. Machining-induced surface integrity of holes drilled in lead-free brass alloy. *Preced. CIRP* **2020**, *87*, 148–152. [CrossRef]

18. Zoghipour, N.; Atay, G.; Kaynak, Y. Modeling and optimization of drilling operation of lead-free brass alloys considering various cutting tool geometries and copper content. *Procedia CIRP* **2021**, *102*, 246–251. [CrossRef]
19. Liu, C.; Yin, Y.; Li, C.; Xu, M.; Li, R.; Chen, Q. Properties of lead-free copper matrix composites prepared through in situ Ni-coated FeS surface modification and mechanical alloying. *J. Alloy. Compd.* **2021**, *881*, 160580. [CrossRef]
20. Vikas, R.D.; Anurag, K.; Atharva, K. Failure analysis of Taper-Lock bush used in aggregate batcher plant for construction applications. *Eng. Fail. Anal.* **2021**, *130*, 105753.
21. Amanov, A.; Cho, I.S.; Kim, D.E. Effectiveness of high-frequency ultrasonic peening treatment on the tribological characteristics of Cu-based sintered materials on steel substrate. *Mater. Des.* **2013**, *45*, 118–124. [CrossRef]
22. Amanov, A.; Pyun, Y.S.; Sasaki, S. Effect of ultrasonic nanocrystalline surface modification (UNSM) technique on the tribological behavior of sintered Cu-based alloy. *Tribol. Int.* **2014**, *72*, 187–197. [CrossRef]
23. Oksanen, V.T.; Lehtovaara, A.J.; Kallio, M.H. Load capacity of lubricated bismuth bronze bimetal bearing under elliptical sliding motion. *Wear* **2017**, *388–889*, 72–80. [CrossRef]
24. Wang, Z.M.; Yang, Q.; Sun, Z.P.; Zhang, B.R.; Zhao, W.; Rao, W.F. The effect of Bi amd Pb on the soft phase in $Al_{82}Sn_{15}Si_{2.2}Cu_{0.8}$ sliding bearing alloy. *Mater. Charact.* **2020**, *170*, 110684. [CrossRef]
25. Lee, C.S.; Kim, H.J.; Amanov, A.; Choo, J.H.; Kim, Y.P.; Cho, I.S. Investigation on very high cycle fatigue of PA66-GF30 GFRP based on fiber orientation. *Compos. Sci. Technol.* **2019**, *180*, 94–100. [CrossRef]
26. Chirikov, V.A.; Dimitrov, D.M.; Boyadjiev, Y.S. Determination of the Dynamic Young's Modulus and Poisson's Ration Based on Higher Frequencies of Beam Transverse Vibration. *Procedia Manuf.* **2020**, *46*, 87–94. [CrossRef]
27. Wang, Z. A new dynamic testing method for elastic, shear modulus and Poisson's ration of concrete. *Constr. Build. Mater.* **2015**, *100*, 129–135. [CrossRef]
28. Amanov, A. Microstructural evolution and mechanical properties of Cu-based alloy by post-sintering ultrasonic nanocrystal surface modification. *Mater. Lett.* **2022**, *308*, 131124. [CrossRef]